



HAL
open science

Multi-Segment Earthquake Clustering as Inferred From 36Cl Exposure Dating, the Bet Kerem Fault System, Northern Israel

R. Dawood, A. Matmon, L. Benedetti, Aster Team, S. Siman-Tov

► **To cite this version:**

R. Dawood, A. Matmon, L. Benedetti, Aster Team, S. Siman-Tov. Multi-Segment Earthquake Clustering as Inferred From 36Cl Exposure Dating, the Bet Kerem Fault System, Northern Israel. *Tectonics*, 2024, 43 (5), 10.1029/2023TC007953 . insu-04721424

HAL Id: insu-04721424

<https://insu.hal.science/insu-04721424v1>

Submitted on 4 Oct 2024

HAL is a multi-disciplinary open access archive for the deposit and dissemination of scientific research documents, whether they are published or not. The documents may come from teaching and research institutions in France or abroad, or from public or private research centers.

L'archive ouverte pluridisciplinaire **HAL**, est destinée au dépôt et à la diffusion de documents scientifiques de niveau recherche, publiés ou non, émanant des établissements d'enseignement et de recherche français ou étrangers, des laboratoires publics ou privés.



Distributed under a Creative Commons Attribution 4.0 International License

List of group authors for ASTER (Accélérateur pour les Sciences de la Terre) Team includes: R. Braucher, D. L. Bourlès, M. Arnold, G. Aumaître, K. Keddadouche.

Key Points:

- The earthquake history of three normal fault segments is reconstructed with ³⁶Cl exposure dating
- Over the last 30 ka, the three fault segments ruptured the earth's surface simultaneously in at least three distinguished periods
- During each activity period, at least two earthquakes occurred very closely in time, each resulting in a rupture of the three segments

Supporting Information:

Supporting Information may be found in the online version of this article.

Correspondence to:

R. Dawood,
rawi.dawood@mail.huji.ac.il

Citation:

Dawood, R., Matmon, A., Benedetti, L., ASTER Team, & Siman-Tov, S. (2024). Multi-segment earthquake clustering as inferred from ³⁶Cl exposure dating, the Bet Kerem fault system, northern Israel. *Tectonics*, 43, e2023TC007953. <https://doi.org/10.1029/2023TC007953>




Received 7 JUN 2023
Accepted 21 MAR 2024

Author Contributions:

Conceptualization: R. Dawood
Supervision: A. Matmon, S. Siman-Tov
Writing – original draft: R. Dawood, A. Matmon, S. Siman-Tov
Writing – review & editing: R. Dawood, A. Matmon, S. Siman-Tov

© Wiley Periodicals LLC. The Authors. This is an open access article under the terms of the [Creative Commons Attribution License](#), which permits use, distribution and reproduction in any medium, provided the original work is properly cited.

Multi-Segment Earthquake Clustering as Inferred From ³⁶Cl Exposure Dating, the Bet Kerem Fault System, Northern Israel

R. Dawood^{1,2} , A. Matmon¹, L. Benedetti³ , ASTER Team³, and S. Siman-Tov² 

¹Institute of Earth Sciences, The Hebrew University of Jerusalem, Jerusalem, Israel, ²Geological Survey of Israel, Jerusalem, Israel, ³Aix-Marseille Université, Centre National de la Recherche Scientifique (CNRS)–Institut de Recherche pour le Développement (IRD)–Collège de France, UM 34 Centre de Recherche et d'Enseignement de Géosciences de l'Environnement (CEREGE), Aix-en-Provence, France

Abstract Recovering the seismic history of multiple segments within a fault system provides a spatiotemporal framework for the fault activity across the system. This kind of data is essential for improving our understanding of how faults interact during earthquake cycles and how they are distributed within a fault system. Bedrock fault scarps, reaching up to 10-m height, are abundant across the Bet Kerem fault system, Galilee, northern Israel. Using the ³⁶Cl exposure dating method, we recovered the last 30 ka scarp exhumation history of three fault segments from the Bet Kerem fault system. Results indicate that the three faults were active simultaneously in at least three distinguished activity periods, during which a minimum of 1.2 m of surface rupturing occurred in each period. The synchronized activity and total surface rupture at each activity period suggest that the three dated segments were ruptured simultaneously by the same earthquake. That is, a multi-segment rupture earthquake and that each activity period included a cluster of at least two large multi-segment earthquakes. The results also indicate a recurrence interval between clusters of 3.5–4.5 ka and the existence of a seismic super cycle with a recurrence interval of about 13 ka.

Plain Language Summary Surface rupture occurs when a large earthquake caused by movement along a fault, breaks through the Earth's surface. The ³⁶Cl cosmogenic dating is used to recover past earthquakes that generate surface rupture. Using this method to constrain the fault activity over multiple earthquake cycles and across fault systems provides essential data to understand how earthquakes behave along fault systems and how faults interact during the earthquakes. We recovered the last 30 ka surface rupture history of three fault segments, each approximately 5 km in length, from the Bet Kerem fault system, northern Israel, using the ³⁶Cl exposure dating method. Results indicate that the three segments were active in at least three distinguished periods, in each of which a minimum of 1.2 m of surface rupturing occurred at each fault segment. The amount of surface rupture observed at each of the segments is too large to be generated by one single earthquake that only ruptures the fault segment. However, when all segments are considered together their total length corresponds well with the amount of offset. We, therefore, suggest that the large surface rupture observed at each activity period is caused by large earthquakes that ruptured the three dated segments at once.

1. Introduction

Constraining fault activity over multiple earthquake cycles and across fault segments in a system is crucial in answering some fundamental questions in the field of earthquakes and faulting. For example, how do different fault segments in a single system interact during the seismic cycles? (Barras et al., 2023; Cowie et al., 2017; Mueller, 2017; Nicol et al., 2010; Nixon et al., 2016) How strain is accumulated and released among different segments within the fault system? (Ferry et al., 2011; Nicol et al., 2010), and how do earthquakes that cause surface rupture behave in fault systems: Do they tend to cluster in time? Does each earthquake rupture multiple segments or just a single segment in the fault system? (Benedetti et al., 2013; Schlagenhauf et al., 2011). Several methods are used to determine the Late Pleistocene–Holocene fault activity as well as the earthquake magnitudes and recurrence intervals. These include written historical records (Guidobon & Stucchi, 1993; Zohar et al., 2017), analyses of damage to historical and archeological sites (Ferrario et al., 2020; Marco, 2008), investigations of seismic trenches (Duross et al., 2016; Reches & Hoexter, 1981; Rockwell & Ben-Zion, 2007; Wechsler et al., 2018), and recovering the seismic exhumation history of carbonated bedrock fault scarps using

^{36}Cl cosmogenic exposure dating methods (Benedetti et al., 2013; Harbor, 1997; Iezzi et al., 2021; Mitchell et al., 2001; Mozafari et al., 2022; Robertson et al., 2020; Schlagenhauf et al., 2010, 2011).

The ^{36}Cl cosmogenic exposure dating method was developed and applied on carbonate normal fault scarps over the last two decades (Akçar et al., 2012; Benedetti et al., 2002; Goodall et al., 2021; Iezzi et al., 2021; Mitchell et al., 2001; Mozafari et al., 2022; Schlagenhauf et al., 2010; Zreda & Noller, 1998). This method is based on the fact that the cosmogenic isotope ^{36}Cl is primarily produced and accumulated in the carbonate fault rocks due to the interaction between cosmic radiation and Ca-rich minerals (Gosse & Phillips, 2001). This production of ^{36}Cl atoms in the fault rocks allows to determine the exhumation history of the scarp during Late Pleistocene to Holocene periods. Hence, both, the ages and magnitudes of the surface slip are obtained for the most recent earthquakes that exhumed the exposed fault scarp (Mitchell et al., 2001; Schlagenhauf et al., 2010).

Interestingly, previous studies that used the same dating method to reveal the seismic exhumation history of fault scarps, showed the occurrence of large displacements (surface slip) on relatively short fault segments (e.g., Benedetti et al., 2002; Mitchell et al., 2001; Schlagenhauf et al., 2010). These results are in contrast to the well-known empirical scaling relation that link large displacements with long surface ruptures (e.g., Wells & Coppersmith, 1994; Wesnousky, 2008). This discrepancy can be explained in two ways: (a) The measured displacement is the result of a dense sequence of moderate earthquakes along a single fault segment that cannot be distinguished by the cosmogenic exposure age dating, (b) The investigated segment is part of a linked array of segments that ruptured simultaneously during a single earthquake that is, multi-segment earthquake. Consequently, surface slips generated by these earthquakes are proportional to the overall length of the ruptured segments but do not fit to the length of any individual segment. Recent seismic data from linked fault systems show that fault segments tend to rupture together during a single earthquake event, and by that generating a long surface rupture (Abdelmeguid et al., 2023; Bello et al., 2021; Iezzi et al., 2019; Manighetti et al., 2005; Natawidjaja et al., 2021; Villani et al., 2018). An excellent example of multi-segment earthquakes is the Amatrice-Norcia seismic sequence that struck the Mt. Vettore fault system, central Italy, during the years 2016–2017. The seismic sequence consisted of three large magnitude earthquakes ($M_w > 6.0$); each ruptured several small fault segments across the Mt. Vettore fault system. The cumulative surface rupture length of these three events was about 30 km long and a maximum surface slip of 2.4 m (Brozzetti et al., 2019; Civico et al., 2018; Villani et al., 2018). Therefore, if large displacements on short fault segments are the result of multi-segment earthquakes, it is expected that the adjacent linked segments will display both synchronized seismic activity and a large amount of surface slip. Thus, to check such a possibility, a long and continuous paleoseismic record for the adjacent fault segments is required.

Normal fault systems, consisting of relatively short segments (>5 km) with carbonate fault scarps, offer a unique opportunity to investigate whether large amount of surface slip on these short segments results from multi-segment earthquakes or from a dense sequence of moderate earthquakes along a single fault segment. By using the ^{36}Cl cosmogenic exposure dating method we can constrain the fault activity over multiple earthquake cycles and across fault systems. In addition, this spatiotemporal framework of faults activity can be used to provide a quantitative description of earthquake timing and surface slip distribution across a fault system. This data can be used to answer important questions about the interactions between different fault segments throughout seismic cycles, how strain is accumulated and released among different segments within the fault system, and whether earthquakes that cause surface rupture tend to cluster in time.

The Bet Kerem fault system in northern Israel has relatively short segments that are closed with carbonate fault scarps. The Holocene exhumation history of one of these fault scarps, the Nahf East scarp, was recovered by Mitchell et al. (2001) using ^{36}Cl exposure dating method. Results suggest that this fault showed the occurrence of large surface slip on relatively short Nahf East fault segment. This study aims to understand the mechanism behind these large displacements and assess the possibility of multi-segment earthquake ruptures within the Bet Kerem system. We achieve this by utilizing ^{36}Cl exposure dating on two additional fault scarps adjacent to the Nahf East segment. By combining our new data with that of Mitchell et al. (2001), we reconstruct the last 30 ka spatiotemporal framework of seismic activity for these three normal faults. This spatiotemporal framework allows us to examine the intricate interactions between fault segments during earthquake cycles, strain accumulation and release, and potential earthquake clustering. Ultimately, this study sheds light on the temporal and spatial patterns of seismic activity within the region, contributing to a more comprehensive understanding of its seismic hazard

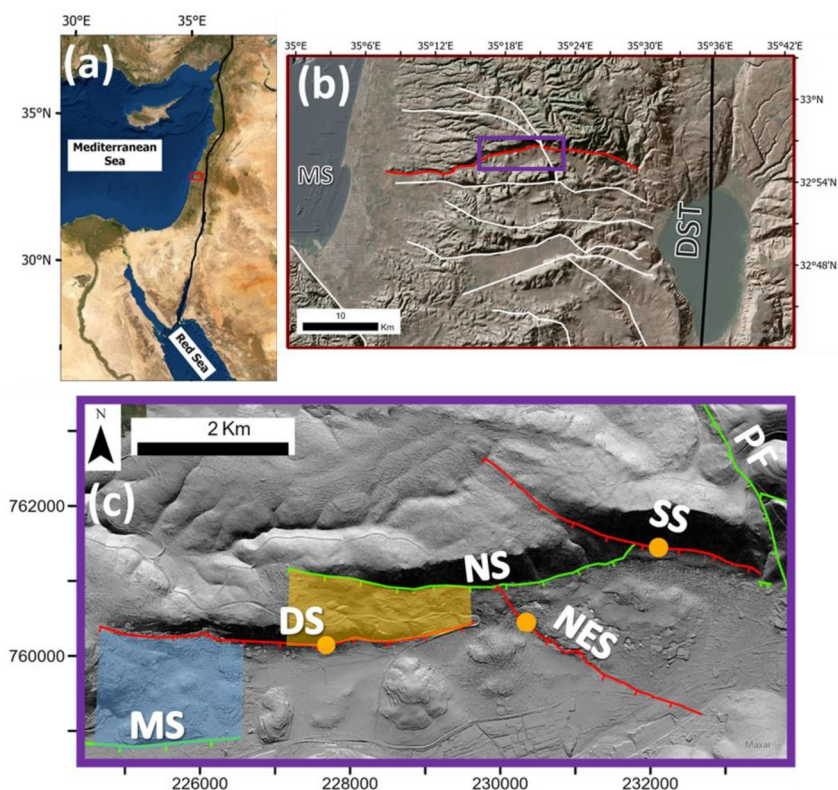


Figure 1. (a) Location of the study area. The central Galilee region is marked with a red open box. (b) Shaded relief map of the central Galilee region, northern Israel (Hall, 1993). White lines outline the major normal fault systems in the Galilee, while a red line highlights the Zurim Escarpment (Sneh et al., 1998) (DST = Dead Sea Transform, MS = Mediterranean Sea). (c) A Shaded relief map of the western half of the Bet Kerem fault system. Red lines indicate the dated segments, sampling sites are marked with orange circles, and the green lines indicate undated segments within the system. (Segments names; PF = Peqi'in fault, SS = Sajur segment, NS = Nahf segment, NES = Nahf East segment, DS = Deir Al-Assad, and MS = Majd al-Krum segment). The two shaded polygons outline the relay ramp zones between the segments: in orange between Nahf and Deir Al-Assad and in blue between Deir Al-Assad and Majd al-Krum segment.

potential. Our findings support the hypothesis that large surface slips on these short segments are the result of multiple earthquakes rupture.

2. Geological Setting

2.1. The Bet Kerem Fault System

The Galilee region, northern Israel is a Mediterranean, mostly mountainous, and densely populated area. It is bounded in the west by the Mediterranean Sea and in the east by the Dead Sea fault (Figure 1). Since the early Pliocene the Galilee has been undergoing N-S extension that is accommodated by normal faulting (Freund, 1970; Matmon et al., 2000; Ron & Eyal, 1985; Wetzler et al., 2022). The Bet Kerem fault system is one of the major fault systems in the Galilee. It is composed of several relatively short (4–7 km) normal fault segments with a general E-W strike (Sneh et al., 1998; Figures 1 and 2). These faults are positioned at an en-echelon pattern and display bedrock scarps, some of which reach 12 m in height (Figures 1 and 2; Figures S1 and S2 in Supporting Information S1) (Freund, 1970; Matmon et al., 2010; Mitchell et al., 2001).

The Holocene exhumation history of one of these fault scarps, the Nahf East scarp, was recovered by Mitchell et al. (2001) using ^{36}Cl exposure dating method. Results show that this fault was active during three distinct periods of intense fault activity with over 6 m of displacement occurring during the middle Holocene. Smaller amounts of displacement (around 1.5 m) occurred during the Late Pleistocene (approximately 12 ka) and late Holocene (approximately 1.5 ka). The length of the Nahf East segment is around 4 km. Assuming that each event ruptured its entire length, one may expect a maximum displacement of several centimeters per earthquake (Wells

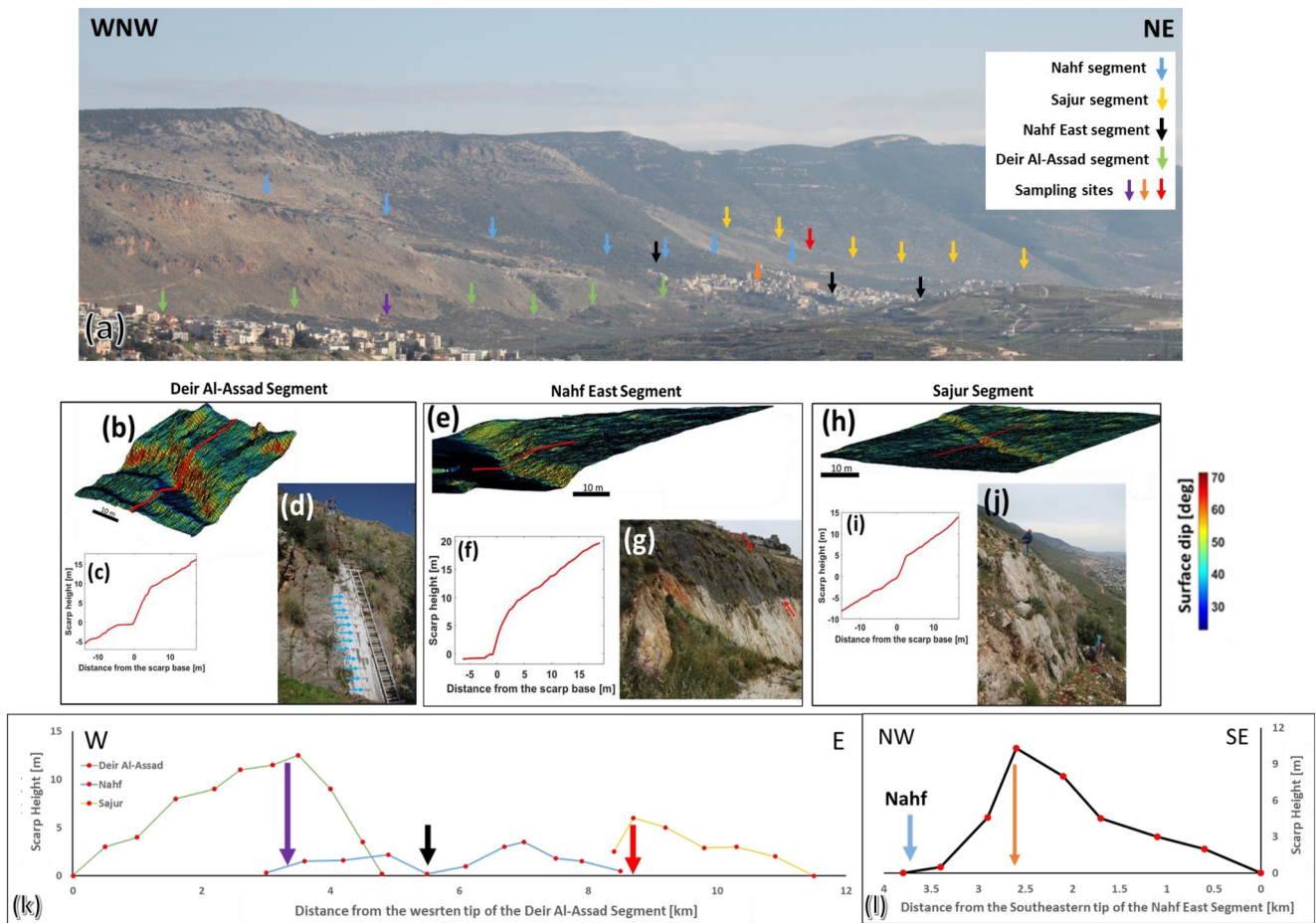


Figure 2. (a) Overall view of the Zurim Escarpment above the Bet Kerem Valley. Arrows outlines the scarp traces of the Sajur segment by yellow arrows, the Nahf segment by blue arrows, the Deir Al-Assad segment by green arrows, and the Nahf East by the black arrows. The red arrow indicates the sampling site at Sajur segment, purple arrow the sampling site at the Deir Al-Assad segment, and orange arrow outlined Mitchell et al. (2001) sampling site at Nahf East segment. (b), (e), and (h) Shaded relief images of the investigated fault scarps. Red lines outline sampling sites and cross section locations. (c), (i) Cross-sections along our sampling sites and (f) at Mitchell et al. (2001) sampling site. (d) Photograph of the sampling site at the Deir Al-Assad segment. Blue arrows indicate sample positions on the scarp. (g) Photograph of Mitchell et al. (2001) sampling site at the Nahf-East Segment. The lower half (white colored) recently exposed by excavations while the greyish, upper half, exposed by earthquake events during the Holocene. Red arrows indicate the section previously sampled by Mitchell et al. (2001). (j) Photograph of our sampling site at the Sajur segment. (k) The along the strike fault scarp height for the Deir Al-Assad segment (green), Nahf segment (blue), and Sajur segment (yellow). The red arrow indicates the sampling site at Sajur segment, purple arrow the sampling site at the Deir Al-Assad segment, and the black arrow outlines the location of the intersection of the Nahf segment with Nahf East segment. (l) The along the strike fault scarp height for the Nahf East segment. The orange arrow outlined Mitchell et al. (2001) sampling site at Nahf East segment, and the blue arrow outlines the location of the intersection of the Nahf East segment with Nahf segment.

& Coppersmith, 1994; Wesnousky, 2008). However, according to the recovered slip history, each of the activity periods caused a displacement of at least 1.5 m (Mitchell et al., 2001). As discussed above, a possible explanation to this discrepancy is that a single strong earthquake ruptured several fault segments within the Bet Kerem fault system, among them the Nahf East segment. Aiming to explore this point, we recovered, using the ^{36}Cl exposure dating method, the exhumation history of the adjacent Sajur and Deir Al-Assad segments (Figures 1 and 2). In addition, we remodeled the exhumation history of the Nahf East segment using the original data by Mitchell et al. (2001) in order to directly compare the exhumation history of the three fault segments.

2.1.1. The Nahf-East Segment

The Nahf East segment is approximately 4.5 km long, with about 3.5 km exposed scarp striking 140° . It is bounded in the north by the Nahf segment and extends to the southeast until it disappears in the Bet Kerem Valley (Figure 1). The along-fault maximum scarp height projection (MSP) displays an asymmetric triangle shape with a maximum scarp height of approximately 10 m, located about 700 m away from the intersection with the Nahf

segment (Figure 2). The studied site of Mitchell et al. (2001) is located close to the scarp height maximum (Figure 2).

2.1.2. The Sajur Segment

The Sajur segment is located east of the Nahf-East segment. This segment strikes 75° and its total length is approximately 6 km. Out of this, a continuous carbonated bedrock fault scarp can be traced for about 3 km, which is considered the segment rupture length (Figure 1). The scarp extends from its eastern tip (close to the Peqi'in fault) and ends abruptly at the intersection with the Nahf segment. The Sajur MSP shows an asymmetric triangle shape with a maximum height of 5.6 m located close to the intersection with the Nahf segment. The location of maximum scarp height is also where we sampled the fault for ^{36}Cl age analysis (Figure 2; Figure S1 in Supporting Information S1).

2.1.3. The Nahf Segment

The Nahf segment is located between the Sajur and Deir Al-Assad segments. It starts at the breached Sajur ramp, passes through the intersection with the Nahf East segment and ends westward as the north boundary of a 500 m wide relay ramp zone that separates the Nahf segment from the Deir Al-Assad segment (Figure 1) (Matmon et al., 2010). The Nahf segment strikes 85° and its total length is approximately 7 km, with a continuous carbonated bedrock fault scarp traceable for about 5 km. The scarp starts at the intersection with the Sajur segment in the east and ends westward in the relay ramp zone (Figure 1). The MSP of the Nahf segment shows two asymmetric triangle shapes with peaks located close to the intersection with the Nahf East segment (Figure 2; Figure S2 in Supporting Information S1).

2.1.4. The Deir Al-Assad Segment

The Deir Al-Assad segment is the westernmost segment of the Bet Kerem fault system investigated in this study. Its average strike is 90° and the total length is approximately 5.5 km. The segment is bounded by a relay ramp zone on its eastern end (the south boundary of the ramp) and by a 1 km wide relay ramp zone on its western end separating it from the Majd al-Krum segment (Figure 1) (Matmon et al., 2010). A continuous carbonated bedrock fault scarp of approximately 4.5 km can be traced. The MSP of the Deir Al-Assad segment shows an asymmetric triangle shape with a maximum scarp height of approximately 12 m. Our sampling location is located close to that maximum scarp height (Figure 2; Figure S1 in Supporting Information S1).

3. Methods

3.1. Selected Sites, Field Sampling, Sample Preparation and Analysis

Carbonated bedrock fault scarps can be exhumed both by erosional processes or by earthquakes that rupture the earth's surface. Therefore, it is important to determine the process by which sites selected for sampling were exhumed. The morphology of the Sajur and the Deir Al-Assad scarps suggests that both were exposed seismically rather than by denudation (Figure 2; Figure S1 in Supporting Information S1; Bubeck et al., 2015; Cowie et al., 2017).

For each fault scarp, Sajur and Deir Al-Assad, we selected a suitable cosmogenic sampling site based on the criteria previously suggested by Bubeck et al. (2015), which included: (a) intact footwall and hanging-wall slopes with no evidence of incision; (b) the sample site is located far away from active gullies and major drainages; (c) far away from landslides; and (d) the fault scarp is well preserved. At each sampling site, samples were collected at 30 cm intervals using a rock drill. Samples were collected along a down-dip transects from the exhumed fault scarp, and two samples from the buried part at 30 and 60 cm below the surface. Some samples were horizontally offset from the main vertical sample line to avoid intensely fractured or eroded parts of the fault scarp, as well as parts with obvious secondary precipitation of calcite. Each sample comprises four to six cores, collectively weighing a minimum of 150 g. These cores have a diameter of 2.54 cm and vary in length from 4 to 10 cm. Importantly, all cores within each sample share the same length (Figure 2; Figure S1 in Supporting Information S1). Overall, 60 samples were collected: 38 from the Deir Al-Assad segment and 22 from the Sajur segment. Sample preparation followed the standard method described by Schimmelpennig et al. (2009), and were conducted at the Cosmogenic Isotope Laboratory, Hebrew University of Jerusalem, Israel. Cl isotopic ratios

($^{36}\text{Cl}/^{35}\text{Cl}$, $^{36}\text{Cl}/^{37}\text{Cl}$ and $^{35}\text{Cl}/^{37}\text{Cl}$ ratios) were measured at the accelerator mass spectrometer at ASTER, CEREGE, Aix en Provence, France. Chemical composition of each sample and the composition of the hanging-wall colluvium were determined using ICP-MS, at the Hebrew University of Jerusalem, Israel.

3.2. Modeling the Scarp Exhumation History

The analytical expressions that are typically employed for surface cosmogenic exposure dating cannot be used to recover the exhumation history of the fault scarp. That is because the ^{36}Cl concentration of each sample is the integration of the accumulated isotopes that were produced below and above the surface and affected by the episodic fault motion. Therefore, in order to recover the seismic exhumation history of a fault scarp, it is necessary to use a numerical model. Here we used the numerical model presented by Schlagenhauf et al. (2010) to recover the exhumation history of the studied fault scarps. The model is based on the fact that the ^{36}Cl production profile of the fault surface that is buried under the colluvium has an exponential depth-dependent shape. As a result, the ^{36}Cl concentration profile of the buried fault surface also shows a depth-fading exponential shape. Once an earthquake occurs and exhumes the buried part, the newly exposed section of the fault scarp starts accumulating ^{36}Cl atoms at a constant rate. Due to the constant accumulation rate the ^{36}Cl exponential shape in the newly exposed section will be preserved. Therefore, repeated large earthquakes on the same normal fault, exhumes deeper portions of the fault surface, and the ^{36}Cl concentration profile along the exposed scarp looks as a series of exponential sections separated by discontinuities. These discontinuities reflect hiatuses between major earthquakes or seismic activity periods that produced surface slip, hence providing a measure of the displacement produced by each period of activity. Modeling of the exponential sections separated by discontinuities allows determination of the age of the major past earthquakes or seismic activity periods (Figure S4 in Supporting Information S1).

Following Schlagenhauf et al. (2010) modeling procedure, for each studied scarp we determined the number of major discontinuities, that is, the number of major events according to the ^{36}Cl profile. To find the major discontinuities points in a ^{36}Cl profile, we use a summed probability density function (PDF). The PDF method treats each measurement as a bell-shaped curve with a width of 2σ (sigma), where σ is the uncertainty of the measurement. The summed PDF curve is created by stacking these individual bell-shaped curves. The highest peaks in the summed PDF curve correspond to the concentrations that are most common in the data. These peaks often correspond to the major changes in the ^{36}Cl profile. However, smaller and less noticeable peaks may also be present due to noise or artifacts in the data. This first step is crucial to determine the amount of fault-slip that was generated by each past seismic event.

Next, we obtained the age of each exhumation event by modeling the ^{36}Cl concentration data using the code provided by Schlagenhauf et al. (2010). The code calculates the theoretical ^{36}Cl profile that is expected to develop on the scarp according to sampling site parameters, the chemical compositions of the rock samples (Figure S3, Tables S1 and S2 in Supporting Information S1, Tables S3 and S4), and the exhumation scenario, which consists of the ages of the exhumation events and the surface slip generated at each event. To determine the ages of the exhumation events, we first determine the age of the oldest exhumation event (the portion of the fault scarp between the topmost sample on the scarp and the first discontinuity point on the ^{36}Cl profile) and the preexposure duration, which approximately represents the interseismic time before the oldest determined event. Once we have fitted the theoretical ^{36}Cl profile calculated by the model to the upper section of the fault scarp, we have determined the age of the oldest exhumation event and the preexposure duration. We then model the next exhumation event by modeling the next down-scarp fault section (the section between the topmost discontinuity point and the one below it). We repeat this iterative process for each successive lower section of the fault scarp, progressively advancing toward the comprehensive fitting of the entire ^{36}Cl profile.

We test the quality of the fitting by comparing the theoretical ^{36}Cl profile to the measured one. We use three complementary metrics to compare the two profiles: [a] weighed root mean square (RMSw)—quantifies the fit between modeled and measured concentrations while including the uncertainties of measured ^{36}Cl concentration. [b] Chi-square test (Chi2)—indicates the balance between model improvement and the number of free parameters influencing the improvement. [c] the Akaike Information Criterion (AICc)—a measure of the balance between the model improvement and the number of introduced free parameters (Akaike, 1974). The most likely exhumation scenario is the one that minimizes the difference between the modeled and measured concentration profiles, as quantified by the three metrics in a population of tested exhumation scenarios. As a final step, we

decreased and increased the number of discontinuity points, which was initially determined in the modeling procedure. For each new number of discontinuities, we determined the most likely exhumation scenario using the complementary metrics. The exhumation scenario that shows the lowest complementary metrics, RMSw, Chi2, and AICc values, among all the tested populations of tested exhumation scenarios is chosen as the exhumation scenario of the fault scarp (Figures S5–S8 in Supporting Information S1 illustrate the progressive adjustment of the number of discontinuity points in the ^{36}Cl data set and the modeling of the data set).

The Schlagenhauf et al. (2010) modeling procedure for fault scarp exhumation history requires identifying the major discontinuity points in the ^{36}Cl profile. This process can be subjective, as it relies on the user to interpret the probability density function (PDF) curve. This subjectivity can affect the results of the modeling. To address this issue, we used the Cowie et al. (2017) code, which is a modified version of the Schlagenhauf et al. (2010) code that uses Markov chain Monte Carlo to reconstruct both the slip rate and the number and timing of changes in slip rate of the observed ^{36}Cl measurements without requiring the identification of major discontinuity points in the ^{36}Cl profile. By reconstructing the slip rate history using the Cowie et al. (2017) model, we can convert the slip rate history into a seismic exhumation history. Periods of high slip rate can be interpreted as representing seismically active periods, while periods of nearly zero slip rate can be interpreted as seismically quiescence periods. Therefore, by using the Cowie et al. (2017) code, we were able to test and validate the fault scarp exhumation history that was obtained using the Schlagenhauf et al. (2010) modeling results.

The Cowie et al. (2017) code takes as input the sampling site parameters, the chemical compositions of the rock samples, and the ^{36}Cl concentration and position of each sample on the fault scarp, as in the Schlagenhauf et al. (2010) model (Figure S3, Tables S1 and S2 in Supporting Information S1, Tables S3 and S4). Additionally, the model requires guesses for the maximum scarp age, the elapsed time since the last slip event, and the average slip step. The model generates a slip history and calculates a forward model of ^{36}Cl values for this slip history. The likelihood of the proposed slip history is then calculated by comparing the modeled ^{36}Cl values to the measured data. The algorithm then varies one of the parameters used to define the slip history and runs the forward model again. The new slip history is accepted if it has a higher likelihood than the previous model or if the ratio of new/current likelihood is higher than a random number drawn from a uniform distribution between 0 and 1. Otherwise, the new model is rejected. For each fault scarp, we run the model for 500,000 iterations and remove a burn-in of 50,000 iterations to exclude models that may be affected by the starting parameters. We give the model a maximum scarp age of 40 ka, a minimum age of 500 years, and an average slip step of 30 cm.

Finally, we compared the exhumation histories generated by the Cowie et al. (2017) and Schlagenhauf et al. (2010) models. In instances where the models' results disagreed, we selected the exhumation history with the lowest RMSw, Chi2, and AICc values.

4. Modeling Results

The ^{36}Cl data are plotted as a function of sample height in Figure 3 for the Deir Al-Assad, Sajur, and Nahf East segments. As expected, the ^{36}Cl concentration increases gradually with height at each site, since higher parts of the scarp have been exposed for longer time. Among the three segments, the Deir Al-Assad fault has the lowest ^{36}Cl concentration at a height of 0 m, while the Sajur fault has the highest. At the top of the fault scarp, the Sajur segment shows the lowest ^{36}Cl concentration. However, due to measurement uncertainties, it is challenging to conclusively determine whether the Deir Al-Assad or Nahf East segments has the higher ^{36}Cl concentration.

Following the procedure described above of Schlagenhauf et al. (2010) modeling procedure, we first identify the major discontinuities that shape each ^{36}Cl profile using the PDF curve (Figure 3). Second, we determined the age of each exhumation event by modeling the ^{36}Cl data with the code provided by Schlagenhauf et al. (2010). Finally, we systematically adjusted the number of discontinuity points, and Figure 3 shows the chosen exhumation scenario for each of the three fault scarps. The chosen exhumation scenario for each fault scarp exhibits the lowest values for the complementary metrics RMSw, Chi2, and AICc, among all the examined sets of exhumation scenarios for that fault scarp (Figures S5–S8 in Supporting Information S1 show an example of how the number of discontinuity points in the ^{36}Cl data set was progressively adjusted and how the data set was modeled).

The Schlagenhauf et al. (2010) model revealed that the Sajur segment was exhumed by three events at 11.2 (± 0.5), 7.5 (± 0.5), and 4.2 (± 0.5) ka, with surface slip of 1.5 (± 0.3), 2.5 (± 0.3), and 1.5 (± 0.3) m, respectively, and pre-exposure duration of 15.0 (± 1.0) ka (Figure 3i and Table 1). The Deir Al-Assad segment was exhumed by

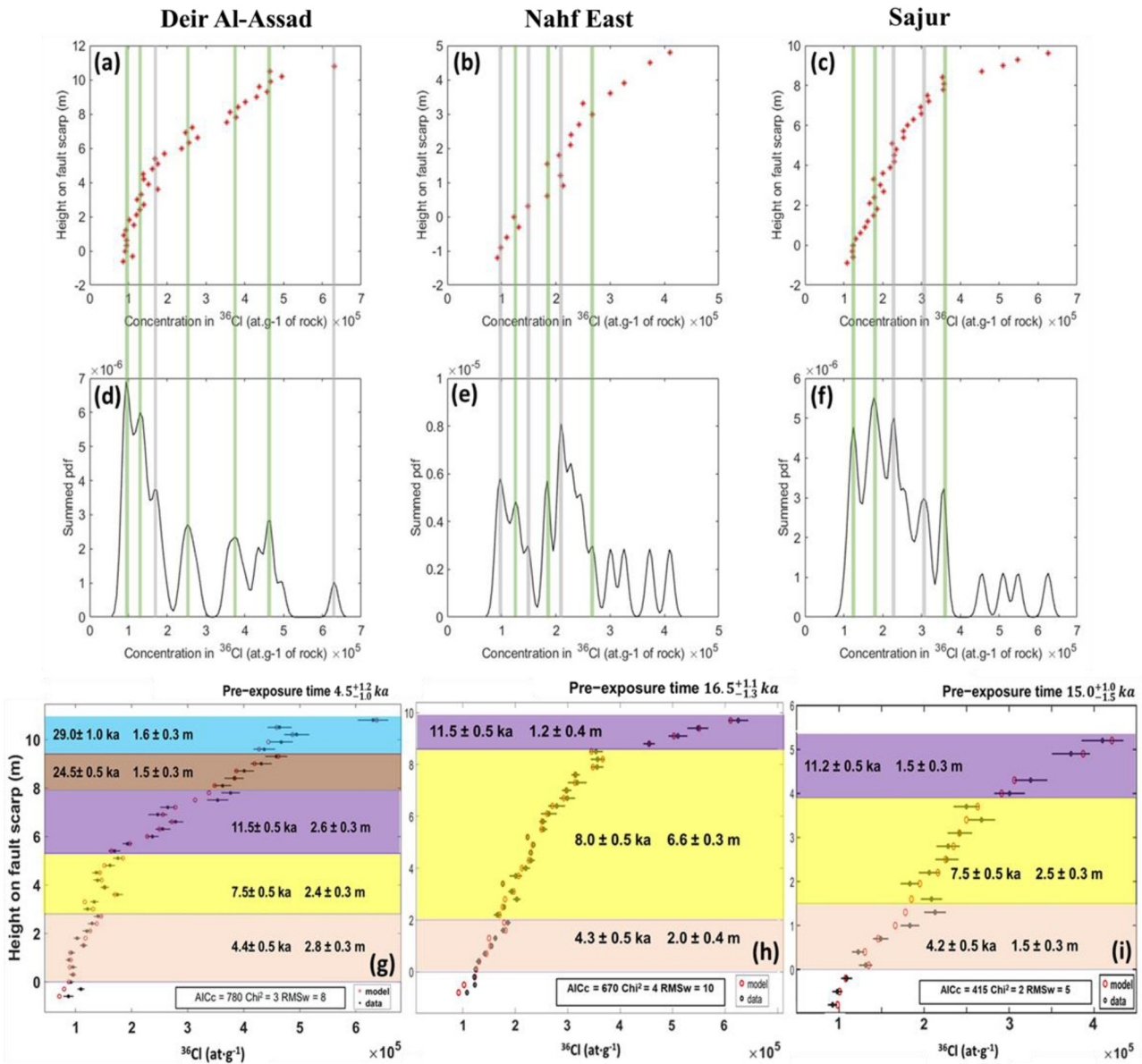


Figure 3. Best models for the three ^{36}Cl profiles. ^{36}Cl data versus scarp height for the Deir Al-Assad (a), Nahf East (b), and Sajur segments (c). Data for the Nahf East segment are from Mitchell et al. (2001). The probability density function (PDF) of the ^{36}Cl data for the Deir Al-Assad (d), Nahf East (e), and Sajur segments (f) shows well-defined peaks that coincide with the discontinuities defined in the ^{36}Cl profiles versus scarp height. Green vertical bars outline well-identified seismic events, and gray bars indicate discontinuities that are not seismic events. (g–i) Shows ^{36}Cl data versus scarp height (black dots) and the best-fit age slip result as obtained by the Schlagenhauf et al. (2010) model (red circles) for the Deir Al-Assad, Nahf East, and Sajur segments, respectively. Event ages and displacements are given per event together with their uncertainties (distinguished by colors).

five events at $29.0 (\pm 1.0)$, $24.5 (\pm 0.5)$, $11.5 (\pm 0.5)$, $7.5 (\pm 0.5)$, and $4.4 (\pm 0.5)$ ka, with surface slip of $1.6 (\pm 0.3)$, $1.5 (\pm 0.3)$, $2.6 (\pm 0.3)$, $2.4 (\pm 0.3)$, and $2.8 (\pm 0.3)$ m, respectively, and pre-exposure duration of $4.5 (\pm 1.2)$ ka (Figure 3g and Table 1). The remolding of the Nahf East segment based on Mitchell et al. (2001) data revealed that the segment was exhumed by three events at $11.5 (\pm 0.5)$, $8.0 (\pm 0.5)$, and $4.3 (\pm 0.5)$ ka, with surface slip of $1.2 (\pm 0.4)$, $6.6 (\pm 0.3)$, and $2.0 (\pm 0.4)$ m, respectively, and pre-exposure duration of $16.5 (\pm 1.3)$ ka (Figure 3h and Table 1).

To ensure that the exhumation scenarios revealed by the Schlagenhauf et al. (2010) model are unbiased, we used the Cowie et al. (2017) model to model and reconstruct the exhumation history of each site, as described in the

Table 1
Surface Rupture Age and Amount at the Three Faults

Period	Fault name	Deir Al-Assad (age/amount of slip)	Nahf east (age/amount of slip)	Sajur (age/amount of slip)
First		4.4 ± 0.5 ka/2.8 m	4.3 ± 0.5 ka/2 m	4.2 ± 0.5 ka/1.5 m
Second		7.5 ± 0.5 ka/2.4 m	8.0 ± 0.5 ka/6.5 m	7.5 ± 0.5 ka/2.5 m
Third		11.5 ± 0.5 ka/2.6 m	11.5 ± 0.5 ka/1.2 m	11.2 ± 0.5 ka/1.5 m
Fourth		24.5 ± 0.5 ka/1.5 m	–	–
Fifth		29 ± 1 ka/1.6 m	–	–
Pre exposure duration		4.4 ^{+1.2} _{-1.0} ka	16.5 ^{+1.1} _{-1.3} ka	15.0 ^{+1.0} _{-1.5} ka

methods section. The Deir Al-Assad site shows five periods of activity at 28.0–31.0, 25.5–26.5, 17.0–10.5, 9.0–7.0, and 5.5–4.2 ka, with surface slip of 1.5, 1.5, 2.4, 2.4, and 2.9 m, respectively (Figure 4a). The Sajur show three period of activity 12.5–11.0, 9.0–7.0, and 5.5–4.2 ka, with surface slip of 1.5, 2.4, and 1.5 m, respectively (Figure 4b). The Nahf East fault shows three periods of activity, each characterized by a different slip rate. The first period, 12.0–9.0 ka, saw 1.5–2.0 m of slip. The second period, 9.0–7.5 ka, was characterized by a high slip rate, with 6–7 m of slip occurring. The third period, 7.5–3.0 ka, saw 2–3 m of slip (Figure 4c).

Both the Cowie et al. (2017) and Schlagenhauf et al. (2010) models agree that the Sajur segment was exhumed by three events. The best exhumation scenario revealed for the Sajur segment by Schlagenhauf et al. (2010) fit well with the 10 best exhumation scenarios for the Sajur segment revealed by Cowie et al. (2017) model. We used the Schlagenhauf et al. (2010) code to compare the quality of fit between the results of the two exhumation models and the measured ³⁶Cl profile using three complementary metrics: RMSw, Chi2, and AICc. The best exhumation scenario for the Sajur segment was exhumation by three events at 11.2 (±0.5), 7.5 (±0.5), and 4.2 (±0.5) ka, with

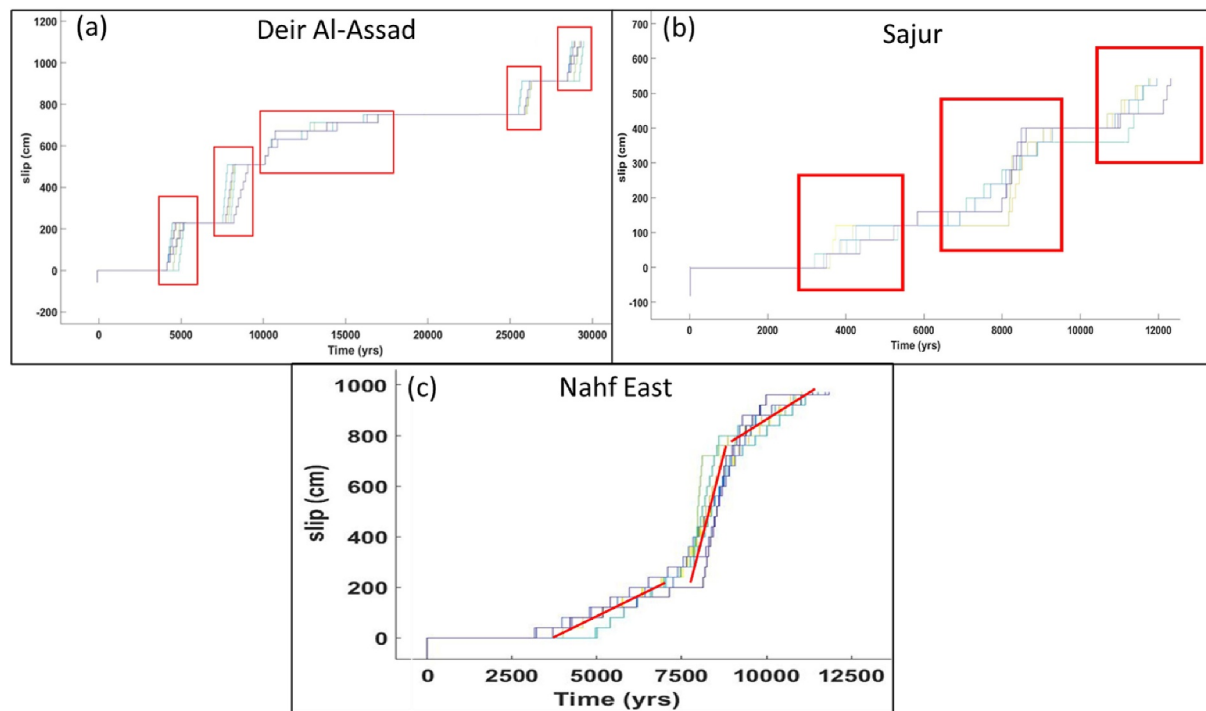


Figure 4. (a) The 10 best exhumation scenarios that revealed by the Markov chain Monte Carlo (MCMC) model for the Deir Al-Assad segment (Each line represents an exhumation scenario). As can be seen, the model result indicates five distinct periods of activity (red boxes). (b) The 10 best exhumation scenarios that revealed by the MCMC model for the Sajur fault segment (Each line represents an exhumation scenario). As can be seen, the model result indicates three distinct periods of activity (red boxes). (c) The 10 best exhumation scenarios that revealed by the MCMC model for the Nahf East segment (Each line represents an exhumation scenario). The model results indicate three periods, each with a different slip rate (red lines).

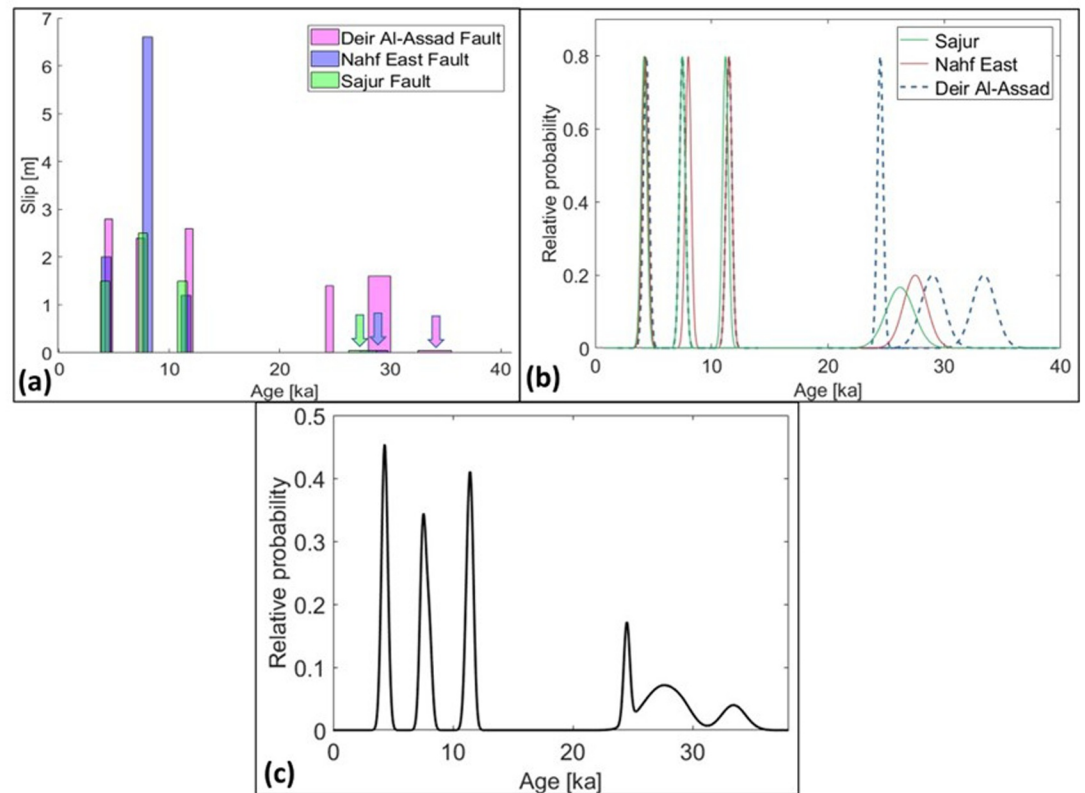


Figure 5. Summary of modeling results. Panel (a): Displacements per event versus time for the three dated faults, with pre-exposure duration outlined by colored arrows. Three distinct periods of synchronized surface rupturing activity are identified, and the pre-exposure duration suggests that the Sajur and Nahf-East segments were also active during the earliest event on the Deir Al-Assad fault. Panel (b): Probability distribution function (PDF) of slip events over time on each of the fault segments. Panel (c): PDF of slip events over time in the Bet Kerem fault system.

surface slip of $1.5 (\pm 0.3)$, $2.5 (\pm 0.3)$, and $1.5 (\pm 0.3)$ m, respectively, and pre-exposure duration of $15.0 (\pm 1.0)$ ka (Figures 3i and 4b and Table 1). The Deir Al-Assad segments show agreement between the best exhumation scenarios revealed by Cowie et al. (2017) and Schlagenhauf et al. (2010) models, respectively, except for the age of the fourth activity period. The Schlagenhauf et al. (2010) model shows that the age is $24.5 (\pm 0.5)$ ka, while the Cowie et al. (2017) model shows an age of 25.5–26.5 ka. The three complementary metrics suggest that the age of the fourth activity period is $24.5 (\pm 0.5)$ ka and that the best exhumation scenario of the Deir Al-Assad segment consists of five events at $29.0 (\pm 1.0)$, $24.5 (\pm 0.5)$, $11.5 (\pm 0.5)$, $7.5 (\pm 0.5)$, and $4.4 (\pm 0.5)$ ka, with surface slip of $1.6 (\pm 0.3)$, $1.5 (\pm 0.3)$, $2.6 (\pm 0.3)$, $2.4 (\pm 0.3)$, and $2.8 (\pm 0.3)$ m, respectively, and pre-exposure duration of $4.5 (\pm 1.2)$ ka (Figures 3g and 4a and Table 1). Both the Cowie et al. (2017) and Schlagenhauf et al. (2010) models agree that the Nahf East segment was exhumed by three events. The best exhumation scenario for the Nahf East segment, as determined by Schlagenhauf et al. (2010), is consistent with the 10 best exhumation scenarios for the Nahf East segment, as determined by the Cowie et al. (2017) model. Using the Schlagenhauf et al. (2010) code, we compared the goodness of fit between the results of the two models and the measured ^{36}Cl profile using three complementary metrics: RMSw, Chi2, and AICc. The best exhumation scenario for the Nahf East segment revealed that the segment was exhumed by three events at $11.5 (\pm 0.5)$, $8.0 (\pm 0.5)$, and $4.3 (\pm 0.5)$ ka, with surface slip of $1.2 (\pm 0.4)$, $6.6 (\pm 0.3)$, and $2.0 (\pm 0.4)$ m, respectively, and a pre-exposure duration of $16.5 (\pm 1.3)$ ka (Figures 3h and 4c and Table 1).

In summary, the three dated fault segments, Nahf-East, Sajur, and Deir Al-Assad, were simultaneously active during three distinct periods through the Late Pleistocene to Holocene: the first period (5.0–4.0 ka), the second period (8.5–7.0 ka), and the third period (12.0–11.0 ka). The slip associated with these events varies from 1.5 to 6.6 m. The Deir Al-Assad segment reveals two additional older periods, which we refer to as the fourth period

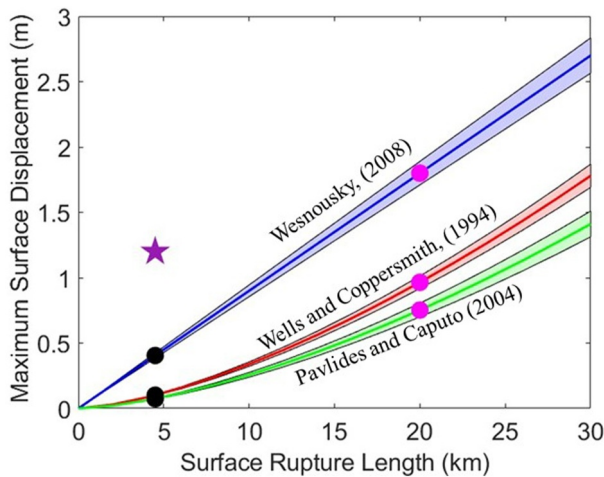


Figure 6. Global empirical relationships between surface rupture length and maximum surface displacement parameters (Pavlides & Caputo, 2004; Wells & Coppersmith, 1994; Wesnousky, 2008). The purple star indicates the minimum observed surface displacement along the studied segments, black dots indicate the maximum surface displacement expected by a rupture length of 4.5 km for the different models, and pink dots indicate the maximum surface displacement that can be generated by a rupture length of 17 km.

(25.0–24.0 ka) and the fifth period (30–28 ka), each of which shows approximately 1.5 m of slip (Figure 5 and Table 1).

5. Discussion

5.1. Limitations of Data and Modeling

Before we discuss the results, it is important to note, that due to the limitation of the ^{36}Cl approach, seismic events that generate less than 25 cm of surface rupture with a recurrence time of less than a few hundred years, cannot be separated as distinguished events. Therefore, the number of events indicated for each segment is a minimum value. This implies that some so-called “events” may in fact include several earthquakes that occurred within a few hundreds of years or one single event that generated a large amount of slip (Schlagenhauf et al., 2010). Hence, we will refer to the scarp exhumation events as activity period.

5.2. The Spatiotemporal Faults Activity

The three studied fault segments show simultaneous activity during three distinct periods during the Holocene and the very Late Pleistocene (12.0–11.0, 8.5–7.0, 5.0–4.0 ka; Figure 5, Table 1). The recurrence interval during this period was approximately 4 ka. This simultaneous activity indicates that the segments interacted with each other, accumulated and released strain during the same periods through the Holocene (Cowie, 1998; Cowie &

Roberts, 2001; Scholz, 2019). In addition to the Holocene activity periods, the Deir Al-Assad segment shows two older periods of activity (25.0–24.0, 30–28 ka; Figures 5 and 6, Table 1). The recurrence interval between these two events is approximately 4 ka, suggests that the recurrence interval between events didn't change despite of the 13 ka seismic quietness between these older periods and the Holocene activity periods.

The pre-exposure duration, which approximately represents the interseismic time before the oldest activity period, of the Sajur and Nahf East segments indicates that these segments were active sometime during 29.5–26.0 and 28.5–25 ka, respectively. These times correspond to the oldest activity periods of the Deir Al-Assad segment. Therefore, it appears that the Sajur and Nahf East segments were also seismically quiescent for approximately 13 ka prior to the 11–12 ka activity period (Figure 5 and Table 1). It is also likely that the three fault segments were active simultaneously during one or both activity periods, similar to what occurred during the Holocene.

Considering the recurrence interval of the Holocene activity periods, along with the surface slip amount during the fourth and fifth activity periods, it appears that the Deir Al-Assad fault activity periods in the Holocene exhibited a recurrence interval of approximately 4 ka and surface slip of about 2.5 m and during the fourth and fifth activity periods (Late Pleistocene) had a recurrence interval of approximately 4 ka and a surface slip of around 1.5 m. The Sajur fault segment's first and third activity periods produced roughly the same amount of surface slip, approximately 1.5 m each, while the second activity period generated around 2.5 m of surface slip (Table 1). Thus, the surface slip amounts for each activity period are less consistent than those of the Deir Al-Assad fault segment, despite having a relatively consistent recurrence interval. The Nahf East segment's surface slip amount ranges widely between 1.2 and 6.5 m, with no clear pattern or characterization evident (Figure 5 and Table 1). In summary except for the second activity period (8.5–7.0 ka), during which the Nahf East segment shows the largest surface slip amount, the Deir Al-Assad segment shows the second largest surface slip amount among the studied segments.

5.3. Earthquakes Magnitude and Recurrence Interval in the Bet Kerem Fault System

Our results suggest the amount of surface slip that occurred at each of the dated faults during each activity period. However, our results do not directly provide information about the number of earthquakes during an activity period, earthquake magnitude, surface rupture length, or maximum surface slip generated by each earthquake. Currently, there is no direct paleoseismological technique that can accurately determine all these parameters. However, the probable magnitude, surface rupture length, and maximum surface slip can be approximated using

empirical relationships that link earthquake magnitude to surface rupture length and maximum surface slip. Therefore, if we determine one of these parameters, we can use these empirical relationships to determine the two other missing parameters.

The studied fault scarps are all less than 4.5 km long (Figures 1 and 2). Based on empirical relationships, earthquakes that rupture short faults are expected to produce surface displacements of 10–30 cm and have a magnitude of approximately 5.5 (Figure 6) (Pavlidis & Caputo, 2004; Wells & Coppersmith, 1994; Wesnousky, 2008). However, the smallest observed surface rupture on each of the studied fault segments is more than 1.2 m (Figure 5 and Table 1). This suggests that the large amounts of surface slip observed on these faults are likely not caused by a single earthquake rupturing the entire fault segment. Therefore, these large amounts of surface slip along relatively short fault segments can be generated in two ways: (a) The measured fault-slip is generated by a dense sequence of moderate (magnitude around 5.5) along a single segment, (b) The investigated segment is part of a linked fault array that ruptured the Earth's surface simultaneously during a single earthquake that is, multi-segment earthquake. If the first mechanism is true, at least four earthquakes would have had to occur on each segment during an activity period. However, earthquakes that rupture only single, short fault segments (5–10 km long) rarely cause surface ruptures at all. Even when they do, the maximum surface slip is only a few centimeters. This is despite existing models suggesting that these fault segments are capable of generating a maximum surface slip of 10–30 cm (Abdelmeguid et al., 2023; Manighetti et al., 2005; Natawidjaja et al., 2021; Pavlidis & Caputo, 2004; Wells & Coppersmith, 1994; Wesnousky, 2008). Therefore, many more than four earthquakes must have occurred along each segment during each activity period to generate the observed surface displacement. The rare occurrence of relatively short (4–5 km) surface rupture by earthquakes and the large number of earthquakes required to generate the observed displacement make it very unlikely that this is the case for the Bet Kerem fault system.

Multi-segment earthquakes are the most common type of earthquake to generate surface rupture in normal fault systems. These earthquakes rupture multiple segments at once, resulting in long surface rupture lengths and large amounts of surface slip (Abdelmeguid et al., 2023; Bello et al., 2021; Bernard & Zollo, 1989; Chiaraluce et al., 2017; Iezzi et al., 2019; Manighetti et al., 2005; Natawidjaja et al., 2021; Wells & Coppersmith, 1994; Wesnousky, 2008). Our data show that the dated fault segments in the Bet Kerem fault system experienced synchronized activity periods, and that the large observed surface displacement is consistent with the occurrence of multi-segment earthquakes (Figure 5 and table 1). The along-fault maximum scarp height projection (MSP) (Figure 2) also supports multi-segment rupture. Fault segments ruptured by multi-segment earthquakes commonly show a scalene triangle shape of the MSP (Manighetti et al., 2005, 2007, 2009; Wesnousky, 2008), which is also observed in the MSP of the dated segments (Figure 2). Therefore, the dated fault segments in the Bet Kerem fault system were likely ruptured by multi-segment earthquakes. In general, considering all the above mentioned observations, one can suggest that for similar cases of normal fault systems, where paleoseismological data shows large surface slip (>1 m) on relatively short faults (<5 km) they were likely ruptured by multi-segment earthquakes.

Based on the previously suggested empirical relationships, we hypothesize that multi-segment earthquakes in the Bet Kerem fault system typically have a magnitude of 6.5, surface rupture length of approximately 17 km, and surface slip of 0.7–1.5 m (Pavlidis & Caputo, 2004; Wells & Coppersmith, 1994; Wesnousky, 2008). We estimate the 17 km long surface rupture based on the combined length of the three dated fault segments and the Nahf segment, which are the four fault segments that exhibit seismically exhumed fault scarps in the Bet Kerem fault system (Figures 1, 2, and 6) (Bhat et al., 2007; Scholz, 2019). Using empirical relationship models, we estimate both the surface slip and the magnitude of the earthquake based on this length (Pavlidis & Caputo, 2004; Wells & Coppersmith, 1994; Wesnousky, 2008). It is worth noting that if the length of the surface rupture is actually smaller, both the surface slip and the magnitude of the earthquake will also be smaller and vice versa.

To estimate the minimum number of earthquakes within each activity period, it is essential to determine the maximum surface slip that occurred at each period. Analysis of surface ruptures caused by earthquakes reveals that the distribution of surface rupture along a fault follows the shape of the fault scarp. For instance, if the fault scarp profile resembles a scalene triangle, the distribution of surface rupture magnitude along the fault will also exhibit a scalene triangle shape, with the maximum surface slip occurring at the point where the fault scarp is highest (Iezzi et al., 2019; Puliti et al., 2020). Our two sampling sites, as well as the Mitchell et al. (2001) sampling site are located close to the maximum height of the fault scarp (Figure 2). Consequently, the sampling sites show



Figure 7. (a) The location of Kabri castle (blue star) relative to the Bet-Kerem fault system (blue triangle), the Dead Sea Transform (DST), and the Carmel Fault (CF). (b) Zoom in on the Bet-Kerem fault system, showing the location of the faults, outlined by colored lines: blue = Sajur segment, green = Nahf East segment, black = Deir Al-Assad segment, and red = Nahf segment, relative to the location of Peki'in cave (red point) and Kabri castle (blue star).

the maximum surface slip that generated at each activity period along each of the segment. Based on that, we assume that the largest surface slip observed during each of the activity period is a good indicator of the maximum surface slip that occurred during that period.

During the first activity period (4–5 ka), the largest surface slip recorded was 2.8 m (Table 1). This suggests that at least two to four earthquakes occurred during this time, based on known correlations between surface slip and rupture length, which indicate that a 17-km-long surface rupture would produce a surface slip of 0.7–1.5 m (Figure 6). Similarly, maximum surface slip observations from other activity periods indicate that at least 4–10 earthquakes occurred during the second activity period, two to four earthquakes occurred during the third activity period, and at least two earthquakes occurred during the fourth and fifth periods.

The time between earthquakes within an active period was too short (hundreds of years at most) to be accurately determined using ^{36}Cl exposure age dating method. Therefore, each activity period likely represents a distinct earthquake cluster. The recurrence interval of these clusters is estimated to range from 3.5 to 5 thousand years during the Holocene and the very Late Pleistocene and between the fifth and fourth activity periods along the Deir Al-Assad segment (Figure 5, Table 1). Notably, there was a period of approximately 13 thousand years without earthquakes between the fourth and third activity periods in the Deir Al-Assad segment. This period of inactivity coincides with the pre-exposure duration observed on the Sajur and Nahf east segments (Figure 5 and Table 1).

Our results, therefore, point to three superimposed recurrence interval wavelengths on the Bet Kerem fault system:

1. Maximum a few 100's of years interval, which separates between discrete earthquakes within a cluster (activity period).
2. A 3.5–5 ka interval between activity periods during the Holocene and Late Pleistocene (activity cycle).
3. An approximately 13 ka interval of total quiescence, that separates between activity cycles.

This phenomenon of the long quiescence period, followed by an activity cycle during which the faults release the strain that has been accumulated during the long quiescence period has been observed in other paleoseismological studies (e.g., Friedrich et al., 2003; Marco et al., 1996; Rockwell et al., 2000; Schlagenhauf et al., 2011), and referred to as “earthquake supercycles” (Salditch et al., 2020). Thus, earthquakes within the Bet Kerem fault system seem to follow the supercycle pattern.

5.4. Archeological Evidence of Past Earthquakes in the Region

Evidence from the archeological record around the Bet Kerem fault system suggests two distinct seismic events, likely caused by earthquakes along the fault system. The first event, roughly 16 km northwest of the fault system, damaged a castle near Kibbutz Kabri (Figure 7). This shaking has been interpreted as a seismic event with an age of 3.8–3.7 ka (Lazar et al., 2020). The age of this shaking event aligns with the first activity period of the Bet Kerem fault system (Table 1), indicating that it may have been caused by earthquakes along the Bet Kerem fault system.

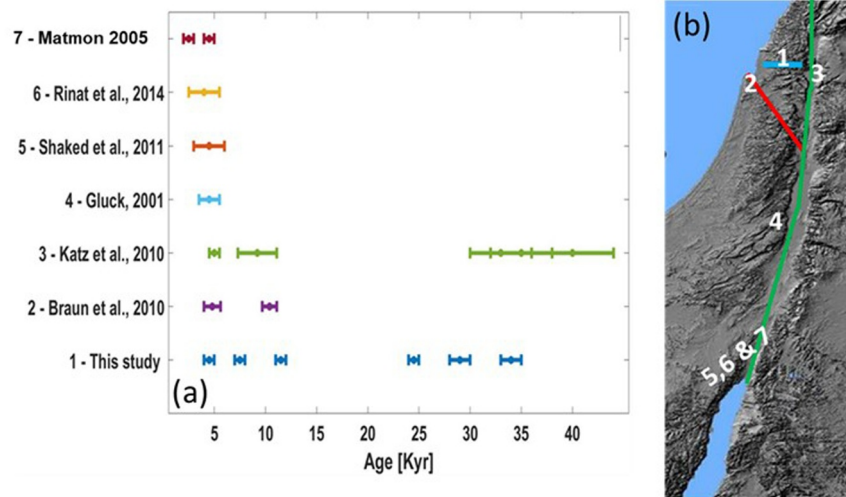


Figure 8. (a) Evidence of seismic events from paleoseismic records along the Dead Sea Transform and the Camel fault. Blue points outline the seismic activity along the Bet-Kerem fault system. As can be seen, some of the events at the Bet-Kerem fault system are synchronized with events along the Dead Sea Transform and the Camel fault. (b) Digital shaded relief (Hall, 1993), with locations of sites mentioned in (a). The green line indicates the Dead Sea Transform, the red line indicates the Carmel fault, and the blue line indicates the Bet-Kerem fault system.

The second event is evident in the Peqi'in Cave, located 5–4 km north of the fault (Figure 7). Here, evidence suggests a collapse involving cave debris and speleothems, possibly triggered by a strong earthquake that occurred sometime after 6.5 ka (Bar-Matthews et al., 2003; Harney et al., 2018). While this age doesn't match any known activity period (Table 1), the collapse could be linked to the first activity period or an earthquake along the fault that didn't produce a surface rupture detectable by the applied ^{36}Cl dating method. It is worth noting that the two recorded events, the collapse of Peqi'in Cave and the damage to Kabri castle, could have been caused by earthquakes along the Dead Sea Transform rather than the Bet Kerem fault system. While we cannot definitively determine which fault system was the source of the earthquakes, the temporal association between the seismic events to the timing of the Bet Kerem fault system earthquakes, as well as their spatial proximity (compared to the Dead Sea Transform), suggest that the Bet Kerem fault system is the more likely source of these events.

5.5. Relations With Past Seismic Events Along the Dead Sea Transform

The seismic activity recorded along the Bet Kerem fault system exhibits a close correlation with periods of intense seismic activity along the Dead Sea Transform. The earliest recorded activity along the Bet Kerem fault system coincides with a series of earthquakes along the Dead Sea Transform and its branching Carmel Fault (CF), which occurred approximately 4–5 ka (Braun et al., 2009; Gluck, 2001; Katz et al., 2009; Matmon et al., 2006; Rinat et al., 2014). Further evidence of this synchronized seismic activity is provided by a shaking event recorded along the CF, dated approximately to 10.4 ± 0.7 ka (Figure 8; Braun et al., 2009), which corresponds to the third activity period at the Bet Kerem fault system. Additionally, records of shaking events along the eastern shore of the Sea of Galilee correlate with periods of intense seismic activity along the Dead Sea Transform (Figure 8). These records include five shaking events, the youngest of which is 4–5 thousand years old and aligns with the first activity period. The remaining four events, of which the most recent is $9,200 \pm 1,900$ years old, could be associated with either the second or third activity period event. The remaining three events have been dated to between 30 and 40 ka (Katz et al., 2009). This period of high seismic activity coincides with the fifth activity periods and the pre-exposure duration along the Deir Al-Assad segment (Figure 8). These observations of synchronized seismic activity between the Bet Kerem fault system and the Dead Sea Transform suggest that earthquakes along the Dead Sea Transform and its branches may trigger seismic activity along the Bet Kerem fault system and vice versa (Scholz, 2010, 2019).

5.6. Implications on Seismic Hazard Assessment

Historical earthquakes along the Dead Sea Transform fault in Israel, such as the 1837 Safed earthquake ($M = 6.4$) and the 1927 Jericho earthquake ($M = 6.2$), have caused significant damage in populated areas (Ben-Menahem, 1981; van Eck & Hofstetter, 1990). Given the high population density of the Bet Kerem Valley, with over 100,000 people, and the potential for large earthquakes (magnitude around 6.5) along the Bet Kerem fault system, the risk of severe damage and casualties is substantial.

The most recent earthquake cluster along the Bet Kerem fault system occurred approximately 4,500 years ago (Figure 5, Table 1). This timeframe falls within the estimated range of recurrence intervals between earthquake clusters during the Holocene to Late Pleistocene eras. This suggests a high likelihood of another earthquake cluster occurring in the near future. However, the extended quiescent period between the third and fourth earthquake clusters, spanning approximately 13,000 years (Figure 5, Table 1), indicates that the Bet Kerem fault system may exhibit supercycle behavior, like other normal fault systems worldwide. In such a scenario, the fault system could have released all accumulated strain and entered into another extended quiescent period, possibly lasting up to 13,000 years. This suggests a low probability of an earthquake cluster occurring in the near future. Given the uncertainty surrounding whether supercycle behavior is characteristic of the Bet Kerem fault system and whether it has entered the long quiescent phase, it appears most likely that the next earthquake cluster will occur within the next 8,000 years.

6. Conclusion

We reconstructed the last 30 ka of seismic exhumation history of three normal fault segments within the Bet Kerem fault system located in the Galilee region, northern Israel, using the ^{36}Cl dating method. Dating results indicate that the three fault segments were active simultaneously during at least three distinguished periods, during which a minimum of 1.2 m of surface rupturing occurred along each of the segments. Since the fault segments are 4.5 km in length, a single earthquake can't generate the observed surface slip and, therefore, a longer fault is required to generate such surface slip. The synchronized activity and the amount of surface rupture generated along each segment at each activity period along with the asymmetric triangle shape of the along-fault maximum scarp height projection, indicate that the investigated segments are a linked fault array that was ruptured simultaneously during each single earthquake that is, multi-segment rupture earthquake. Each of these earthquakes was approximately 6.5 in magnitude, generated approximately 17 km of surface rupture length, and 1–1.5 m of surface slip. The maximum observed amount of surface slip during each activity period is much larger than that generated by a single event and, therefore, we conclude that each activity period included a cluster of earthquakes that consist of at least two events. The recurrence interval of these clusters is 3.5–5 ka, but the Bet Kerem fault system also shows a longer quiescence period of about 13 ka between these clusters.

Data Availability Statement

Data and Software Availability Statement: All data are available at the following link <https://doi.org/10.6084/m9.figshare.24714774>. The Nahf East ^{36}Cl data are available through Mitchell et al. (2001) at <https://doi.org/10.1029/2000jb900373>. **Software:** The ^{36}Cl fault scarp exhumation models are available through Cowie et al. (2017) at <https://doi.org/10.1038/srep44858> and Schlagenhauf et al. (2010) at <https://doi.org/10.1111/j.1365-246X.2010.04622.x>.

References

- Abdelmeguid, M., Zhao, C., Yalcinkaya, E., Gazetas, G., Elbanna, A., & Rosakis, A. (2023). Dynamics of episodic supershear in the 2023 M7.8 Kahramanmaraş/Pazarçik earthquake, revealed by near-field records and computational modeling. *Communications Earth & Environment*, 4(1), 456. <https://doi.org/10.1038/s43247-023-01131-7>
- Akaike, H. (1974). A new look at the statistical model identification. *IEEE Transactions on Automatic Control*, 19(6), 716–723. <https://doi.org/10.1109/TAC.1974.1100705>
- Akçar, N., Tikhomirov, D., Özkaymak, Ç., Ivy-Ochs, S., Alfimov, V., Sözbilir, H., et al. (2012). ^{36}Cl exposure dating of paleoearthquakes in the Eastern Mediterranean: First results from the western Anatolian Extensional Province, Manisa fault zone, Turkey. *Bulletin of the Geological Society of America*, 124(11–12), 1724–1735. <https://doi.org/10.1130/B30614.1>
- Bar-Matthews, M., Ayalon, A., Gilmour, M., Matthews, A., & Hawkesworth, C. J. (2003). Sea—Land oxygen isotopic relationships from planktonic foraminifera and speleothems in the Eastern Mediterranean region and their implication for paleorainfall during interglacial intervals. *Geochimica et Cosmochimica Acta*, 67(17), 3181–3199. [https://doi.org/10.1016/S0016-7037\(02\)01031-1](https://doi.org/10.1016/S0016-7037(02)01031-1)

Acknowledgments

We are grateful to the two anonymous reviewers for their valuable feedback, which significantly improved the quality of this article. We also thank Taylor Schildgen and the Associate Editor for their expert editorial guidance throughout the manuscript preparation process. We extend our sincere appreciation to G. Shraiber, R. Shaar, E. Telg, N. Gazit, N. Moshe, and I. Temkin for their assistance with sample collection and field work. We are also thankful to O. Tirosh, Y. Geller, and Y. Ebert for their contributions to sample preparation and chemical measurements. Fruitful discussions and ideas were provided by A. Agnon, E. Aharonov, O. Katz, and Z. Reches, and we are grateful for their input. Financial support for this research was provided by the Israel Science Foundation Grant 2470/21, the National Steering Committee for Earthquake Preparedness, and a Special Scholarship for M.Sc. students by the Faculty of Sciences, The Hebrew University of Jerusalem.

- Barras, F., Thøgersen, K., Aharonov, E., & Renard, F. (2023). How do earthquakes stop? Insights from a minimal model of frictional rupture. *Journal of Geophysical Research: Solid Earth*, 128(8), e2022JB026070. <https://doi.org/10.1029/2022JB026070>
- Bello, S., Scott, C. P., Ferrarini, F., Brozzetti, F., Scott, T., Cirillo, D., et al. (2021). High-resolution surface faulting from the 1983 Idaho Lost River Fault Mw 6.9 earthquake and previous events. *Scientific Data*, 8(1), 68. <https://doi.org/10.1038/s41597-021-00838-6>
- Benedetti, L., Finkel, R., Papanastassiou, D., King, G., Armijo, R., Ryerson, F., et al. (2002). Post-glacial slip history of the Sparta fault (Greece) determined by ^{36}Cl cosmogenic dating: Evidence for non-periodic earthquakes. *Geophysical Research Letters*, 29(8), 87-1-87-4. <https://doi.org/10.1029/2001gl014510>
- Benedetti, L., Manighetti, L., Gaudemer, Y., Finkel, R., Malavieille, J., Pou, K., et al. (2013). Earthquake synchrony and clustering on Fucino faults (Central Italy) as revealed from in situ ^{36}Cl exposure dating. *Journal of Geophysical Research: Solid Earth*, 118(9), 4948-4974. <https://doi.org/10.1002/jgrb.50299>
- Ben-Menahem, A. (1981). Variation of slip and creep along the Levant Rift over the past 4500 years. *Tectonophysics*, 80(1-4), 183-197. [https://doi.org/10.1016/0040-1951\(81\)90149-9](https://doi.org/10.1016/0040-1951(81)90149-9)
- Bernard, P., & Zollo, A. (1989). The Irpinia (Italy) 1980 earthquake: Detailed analysis of a complex normal faulting. *Journal of Geophysical Research*, 94(B2), 1631-1647. <https://doi.org/10.1029/JB094IB02P01631>
- Bhat, H. S., Olives, M., Dmowska, R., & Rice, J. R. (2007). Role of fault branches in earthquake rupture dynamics. *Journal of Geophysical Research*, 112(11), B11309. <https://doi.org/10.1029/2007JB005027>
- Braun, Y., Kagan, E., Bar-Matthews, M., Ayalon, A., & Agnon, A. (2009). Dating seiploseismites near the Dead Sea Transform and the Carmel Fault: Clues to coupling of a plate boundary and its branch. *Israel Journal of Earth Sciences*, 58(3-4), 257-273. <https://doi.org/10.1560/IJES.58.3-4.257>
- Brozzetti, F., Boncio, P., Cirillo, D., Ferrarini, F., de Nardis, R., Testa, A., et al. (2019). High-resolution field mapping and analysis of the August-October 2016 coseismic surface faulting (Central Italy earthquakes): Slip distribution, parameterization, and comparison with global earthquakes. *Tectonics*, 38(2), 417-439. <https://doi.org/10.1029/2018TC005305>
- Bubeck, A., Wilkinson, M., Roberts, G. P., Cowie, P. A., McCaffrey, K. J. W., Phillips, R., & Sammonds, P. (2015). The tectonic geomorphology of bedrock scarps on active normal faults in the Italian Apennines mapped using combined ground penetrating radar and terrestrial laser scanning. *Geomorphology*, 237, 38-51. <https://doi.org/10.1016/j.geomorph.2014.03.011>
- Chiaraluce, L., Di Stefano, R., Tinti, E., Scognamiglio, L., Michele, M., Casarotti, E., et al. (2017). The 2016 central Italy seismic sequence: A first look at the mainshocks, aftershocks, and source models. *Seismological Research Letters*, 88(3), 757-771. <https://doi.org/10.1785/0220160221>
- Civico, R., Pucci, S., Villani, F., Pizzimenti, L., De Martini, P. M., Nappi, R., et al. (2018). Surface ruptures following the 30 October 2016 Mw 6.5 Norcia earthquake, central Italy. *Journal of Maps*, 14(2), 151-160. <https://doi.org/10.1080/17445647.2018.1441756>
- Cowie, P. (1998). A healing-reloading feedback control on the growth rate of seismogenic faults. *Journal of Structural Geology*, 20(8), 1075-1087. [https://doi.org/10.1016/S0191-8141\(98\)00034-0](https://doi.org/10.1016/S0191-8141(98)00034-0)
- Cowie, P., Phillips, R., Roberts, G., McCaffrey, K., Zijerveld, L., Gregory, L., et al. (2017). Orogen-scale uplift in the central Italian Apennines drives episodic behaviour of earthquake faults. *Scientific Reports*, 7(1), 44858. <https://doi.org/10.1038/srep44858>
- Cowie, P., & Roberts, G. P. (2001). Constraining slip rates and spacings for active normal faults. *Journal of Structural Geology*, 23(12), 1901-1915. [https://doi.org/10.1016/S0191-8141\(01\)00036-0](https://doi.org/10.1016/S0191-8141(01)00036-0)
- Duross, C. B., Personius, S. F., Crone, A. J., Olig, S. S., Hylland, M. D., Lund, W. R., & Schwartz, D. P. (2016). Fault segmentation: New concepts from the Wasatch Fault Zone, Utah, USA. *Journal of Geophysical Research: Solid Earth*, 121(2), 1131-1157. <https://doi.org/10.1002/2015JB012519>
- Ferrario, M. F., Katz, O., Hillman, A., Livio, F., Amit, R., & Michetti, A. M. (2020). The mid-eighth century CE surface faulting along the Dead Sea Fault at Tiberias (Sea of Galilee, Israel). *Tectonics*, 39(9). <https://doi.org/10.1029/2020TC006186>
- Ferry, M., Meghraoui, M., Karaki, N. A., Al-Taj, M., & Khalil, L. (2011). Episodic behavior of the Jordan Valley section of the Dead Sea fault inferred from a 14-ka-long integrated catalog of large earthquakes. *Bulletin of the Seismological Society of America*, 101(1), 39-67. <https://doi.org/10.1785/0120100097>
- Freund, R. (1970). Geometry of faulting in Galilee. *Israel Journal of Earth Sciences*, 19(3-4), 117-140.
- Friedrich, A. M., Wernicke, B. P., Niemi, N. A., Bennett, R. A., & Davis, J. L. (2003). Comparison of geodetic and geologic data from the Wasatch region, Utah, and implications for the spectral character of Earth deformation at periods of 10 to 10 million years. *Journal of Geophysical Research*, 108(B4), 2199. <https://doi.org/10.1029/2001JB000682>
- Gluck, D. (2001). The landscape evolution of the southwestern Dead Sea basin and the paleoseismic record of the southwestern marginal fault of the Dead Sea basin and the Carmel fault during the late Pleistocene and the Holocene. Retrieved from <https://www.gov.il/en/departments/publications/reports/gluck-report-2002>
- Goodall, H. J., Gregory, L. C., Wedmore, L. N. J., McCaffrey, K. J. W., Amey, R. M. J., Roberts, G. P., et al. (2021). Determining histories of slip on normal faults with bedrock scarps using cosmogenic nuclide exposure data. *Tectonics*, 40(3). <https://doi.org/10.1029/2020TC006457>
- Gosse, J. C., & Phillips, F. M. (2001). Terrestrial in situ cosmogenic nuclides: Theory and application. *Quaternary Science Reviews*, 20(14), 1475-1560. [https://doi.org/10.1016/S0277-3791\(00\)00171-2](https://doi.org/10.1016/S0277-3791(00)00171-2)
- Guidobon, M., & Stucchi, E. (1993). The contribution of historical records of earthquakes to the evaluation of seismic hazard. *Annals of Geophysics*, 36(3-4). <https://doi.org/10.4401/ag-4264>
- Hall, J. (1993). The GSI digital terrain model (DTM) project completed A 100m bathymetric grid for the seas around the Arabian Plate View project THE GSI DIGITAL TERRAIN MODEL (DTM) PROJECT COMPLETED. *OSI Current Research*, 8. Retrieved from <https://www.researchgate.net/publication/285636952>
- Harbor, D. J. (1997). Landscape evolution at the margin of the basin and range. *Geology*, 25(12), 1111. [https://doi.org/10.1130/0091-7613\(1997\)025<1111:LEATMO>2.3.CO;2](https://doi.org/10.1130/0091-7613(1997)025<1111:LEATMO>2.3.CO;2)
- Harney, É., May, H., Shalem, D., Rohland, N., Mallick, S., Lazaridis, I., et al. (2018). Ancient DNA from Chalcolithic Israel reveals the role of population mixture in cultural transformation. *Nature Communications*, 9(1), 3336. <https://doi.org/10.1038/s41467-018-05649-9>
- Iezzi, F., Roberts, G., Faure Walker, J., Papanikolaou, I., Ganas, A., Deligiannakis, G., et al. (2021). Temporal and spatial earthquake clustering revealed through comparison of millennial strain-rates from ^{36}Cl cosmogenic exposure dating and decadal GPS strain-rate. *Scientific Reports*, 11(1), 23320. <https://doi.org/10.1038/s41598-021-02131-3>
- Iezzi, F., Roberts, G., Walker, J. F., & Papanikolaou, I. (2019). Occurrence of partial and total coseismic ruptures of segmented normal fault systems: Insights from the Central Apennines, Italy. *Journal of Structural Geology*, 126, 83-99. <https://doi.org/10.1016/j.jsg.2019.05.003>
- Katz, O., Amit, R., Yagoda-Biran, G., Hatzor, Y. H., Porat, N., & Medvedev, B. (2009). Quaternary earthquakes and landslides in the Sea of Galilee area, the Dead Sea Transform: Paleoseismic analysis and implication to the current hazard. *Israel Journal of Earth Sciences*, 58(3-4), 275-294. <https://doi.org/10.1560/IJES.58.3-4.275>

- Lazar, M., Cline, E. H., Nickelsberg, R., Shahack-Gross, R., & Yasur-Landau, A. (2020). Earthquake damage as a catalyst to abandonment of a Middle Bronze Age settlement: Tel Kabri, Israel. *PLoS One*, *15*(9), e0239079. <https://doi.org/10.1371/journal.pone.0239079>
- Manighetti, I., Campillo, M., Bouley, S., & Cotton, F. (2007). Earthquake scaling, fault segmentation, and structural maturity. *Earth and Planetary Science Letters*, *253*(3–4), 429–438. <https://doi.org/10.1016/j.epsl.2006.11.004>
- Manighetti, I., Campillo, M., Sammis, C., Mai, P. M., & King, G. (2005). Evidence for self-similar, triangular slip distributions on earthquakes: Implications for earthquake and fault mechanics. *Journal of Geophysical Research*, *110*(B5), B05302. <https://doi.org/10.1029/2004JB003174>
- Manighetti, I., Zigone, D., Campillo, M., & Cotton, F. (2009). Self-similarity of the largest-scale segmentation of the faults: Implications for earthquake behavior. *Earth and Planetary Science Letters*, *288*(3–4), 370–381. <https://doi.org/10.1016/j.epsl.2009.09.040>
- Marco, S. (2008). Recognition of earthquake-related damage in archaeological sites: Examples from the Dead Sea fault zone. *Tectonophysics*, *453*(1–4), 148–156. <https://doi.org/10.1016/j.tecto.2007.04.011>
- Marco, S., Stein, M., Agnon, A., & Ron, H. (1996). Long-term earthquake clustering: A 50,000-year paleoseismic record in the Dead Sea Graben. *Journal of Geophysical Research B: Solid Earth*, *101*(3), 6179–6191. <https://doi.org/10.1029/95jb01587>
- Matmon, A., Katz, O., Shaar, R., Ron, H., Porat, N., & Agnon, A. (2010). Timing of relay ramp growth and normal fault linkage, Upper Galilee, northern Israel. *Tectonics*, *29*(2). <https://doi.org/10.1029/2009TC002510>
- Matmon, A., Shaked, Y., Porat, N., Enzel, Y., Finkel, R., Lifton, N., et al. (2006). Corrigendum to “Landscape development in an hyperarid sandstone environment along the margins of the Dead Sea fault: Implications from dated rock falls”. *Earth and Planetary Science Letters*, *240*(2005), 803–817. <https://doi.org/10.1016/j.epsl.2006.03.013>
- Matmon, A., Zilberman, E., & Enzel, Y. (2000). Determination of escarpment age using morphologic analysis: An example from the Galilee, northern Israel. *GSA Bulletin*, *112*(12), 1864–1876. GeoScienceWorld. [https://doi.org/10.1130/0016-7606\(2000\)112<1864:DOEAUM>2.0.CO;2](https://doi.org/10.1130/0016-7606(2000)112<1864:DOEAUM>2.0.CO;2)
- Mitchell, S. G., Matmon, A., Bierman, P. R., Enzel, Y., Caffee, M., & Rizzo, D. (2001). Displacement history of a limestone normal fault scarp, northern Israel, from cosmogenic ³⁶Cl. *Journal of Geophysical Research*, *106*(B3), 4247–4264. <https://doi.org/10.1029/2000jb900373>
- Mozafari, N., Özkaymak, Ç., Sümer, Ö., Tikhomirov, D., Uzel, B., Yeşilyurt, S., et al. (2022). Seismic history of western Anatolia during the last 16 kyr determined by cosmogenic ³⁶Cl dating. *Swiss Journal of Geosciences*, *115*(1), 5. <https://doi.org/10.1186/s00015-022-00408-x>
- Mueller, K. (2017). Variation in slip rates on active faults: Natural growth or stress transients? *Geology*, *45*(3), 287–288. <https://doi.org/10.1130/focus032017.1>
- Natawidjaja, D. H., Daryono, M. R., Prasetya, G., Liu, P. L. F., Hananto, N. D., Kongko, W., (2021). The 2018 M_w7.5 Palu “supershear” earthquake ruptures geological fault’s multisegment separated by large bends: Results from integrating field measurements, LiDAR, swath bathymetry and seismic-reflection data. *Geophysical Journal International*, *224*(2). <https://doi.org/10.1093/gji/ggaa498>
- Nicol, A., Walsh, J. J., Villamor, P., Seebeck, H., & Berryman, K. R. (2010). Normal fault interactions, paleoearthquakes and growth in an active rift. *Journal of Structural Geology*, *32*(8), 1101–1113. <https://doi.org/10.1016/j.jsg.2010.06.018>
- Nixon, C. W., McNeill, L. C., Bull, J. M., Bell, R. E., Gawthorpe, R. L., Henstock, T. J., et al. (2016). Rapid spatiotemporal variations in rift structure during development of the Corinth Rift, central Greece. *Tectonics*, *35*(5), 1225–1248. <https://doi.org/10.1002/2015TC004026>
- Pavlidis, S., & Caputo, R. (2004). Magnitude versus faults’ surface parameters: Quantitative relationships from the Aegean Region. *Tectonophysics*, *380*(3–4), 159–188. <https://doi.org/10.1016/j.tecto.2003.09.019>
- Puliti, I., Pizzi, A., Benedetti, L., Di Domenica, A., & Fleury, J. (2020). Comparing slip distribution of an active fault system at various timescales: Insights for the evolution of the Mt. Vettore-Mt. Bove fault system in Central Apennines. *Tectonics*, *39*(9), e2020TC006200. <https://doi.org/10.1029/2020TC006200>
- Reches, Z., & Hoexter, D. F. (1981). Holocene seismic and tectonic activity in the Dead Sea area. *Tectonophysics*, *80*(1–4), 235–254. [https://doi.org/10.1016/0040-1951\(81\)90151-7](https://doi.org/10.1016/0040-1951(81)90151-7)
- Rinat, Y., Matmon, A., Arnold, M., Aumaître, G., Bourlès, D., Keddadouche, K., et al. (2014). Holocene rockfalls in the southern Negev Desert, Israel and their relation to Dead Sea fault earthquakes. *Quaternary Research (United States)*, *81*(2), 260–273. <https://doi.org/10.1016/j.yqres.2013.12.008>
- Robertson, J., Roberts, G. P., Iezzi, F., Meschis, M., Gheorghiu, D. M., Sahy, D., et al. (2020). Distributed normal faulting in the tip zone of the South Alkyonides Fault System, Gulf of Corinth, constrained using ³⁶Cl exposure dating of late-Quaternary wave-cut platforms. *Journal of Structural Geology*, *136*, 104063. <https://doi.org/10.1016/j.jsg.2020.104063>
- Rockwell, T. K., & Ben-Zion, Y. (2007). High localization of primary slip zones in large earthquakes from paleoseismic trenches: Observations and implications for earthquake physics. *Journal of Geophysical Research*, *112*(B10), B10304. <https://doi.org/10.1029/2006JB004764>
- Rockwell, T. K., Lindvall, S., Herzberg, M., Murbach, D., Dawson, T., & Berger, G. (2000). Paleoseismology of the Johnson Valley, Kickapoo, and Homestead Valley faults: Clustering of earthquakes in the eastern California shear zone. *Bulletin of the Seismological Society of America*, *90*(5), 1200–1236. <https://doi.org/10.1785/0119990023>
- Ron, H., & Eyal, Y. (1985). Intraplate deformation by block rotation and mesostructures along the Dead Sea Transform, northern Israel. *Tectonics*, *4*(1), 85–105. <https://doi.org/10.1029/TC004i001p00085>
- Salditch, L., Stein, S., Neely, J., Spencer, B. D., Brooks, E. M., Agnon, A., & Liu, M. (2020). Earthquake supercycles and long-term fault memory. *Tectonophysics*, *774*, 228289. <https://doi.org/10.1016/j.tecto.2019.228289>
- Schimmelpfennig, I., Benedetti, L., Finkel, R., Pik, R., Blard, P. H., Bourlès, D., et al. (2009). Sources of in-situ ³⁶Cl in basaltic rocks. Implications for calibration of production rates. *Quaternary Geochronology*, *4*(6), 441–461. <https://doi.org/10.1016/j.quageo.2009.06.003>
- Schlagenhauf, A., Gaudemer, Y., Benedetti, L., Manighetti, I., Palumbo, L., Schimmelpfennig, I., et al. (2010). Using in situ Chlorine-36 cosmocnuclide to recover past earthquake histories on limestone normal fault scarps: A reappraisal of methodology and interpretations. *Geophysical Journal International*, *182*(1), <https://doi.org/10.1111/j.1365-246X.2010.04622.x>
- Schlagenhauf, A., Manighetti, I., Benedetti, L., Gaudemer, Y., Finkel, R., Malavieille, J., & Pou, K. (2011). Earthquake supercycles in Central Italy, inferred from ³⁶Cl exposure dating. *Earth and Planetary Science Letters*, *307*(3–4), 487–500. <https://doi.org/10.1016/j.epsl.2011.05.022>
- Scholz, C. H. (2010). Large earthquake triggering, clustering, and the synchronization of faults. *Bulletin of the Seismological Society of America*, *100*(3), 901–909. <https://doi.org/10.1785/0120090309>
- Scholz, C. H. (2019). *The mechanics of earthquakes and faulting* (3rd ed.). Cambridge University Press. <https://doi.org/10.1017/9781316681473>
- Sneh, A., Bartov, Y., Weissbrod, T., & Rosensaft, M. (1998). *Geological map of Israel, 1:200,000*. Geological Survey of Israel (4 sheets). Retrieved from <https://www.gov.il/he/departments/general/israel-map-1-200k>
- van Eck, T., & Hofstetter, A. (1990). Fault geometry and spatial clustering of microearthquakes along the Dead Sea-Jordan rift fault zone. *Tectonophysics*, *180*(1), 15–27. [https://doi.org/10.1016/0040-1951\(90\)90368-I](https://doi.org/10.1016/0040-1951(90)90368-I)
- Villani, F., Pucci, S., Civico, R., De Martini, P. M., Cinti, F. R., & Pantosti, D. (2018). Surface faulting of the 30 October 2016 M_w 6.5 Central Italy earthquake: Detailed analysis of a complex coseismic rupture. *Tectonics*, *37*(10), 3378–3410. <https://doi.org/10.1029/2018TC005175>

- Wechsler, N., Rockwell, T. K., & Klinger, Y. (2018). Variable slip-rate and slip-per-event on a plate boundary fault: The Dead Sea fault in northern Israel. *Tectonophysics*, 722, 210–226. <https://doi.org/10.1016/j.tecto.2017.10.017>
- Wells, D. L., & Coppersmith, K. J. (1994). New empirical relationships among magnitude, rupture length, rupture width, rupture area, and surface displacement. *Bulletin of the Seismological Society of America*, 84(4), 974–1002. <https://doi.org/10.1785/bssa0840040974>
- Wesnowsky, S. G. (2008). Displacement and geometrical characteristics of earthquake surface ruptures: Issues and implications for seismic-hazard analysis and the process of earthquake rupture. *Bulletin of the Seismological Society of America*, 98(4), 1609–1632. <https://doi.org/10.1785/0120070111>
- Wetzler, N., Segev, A., & Lyakhovsky, V. (2022). Uplift and subsidence at the periphery of the Lebanese Restraining Bend, northern Dead Sea Fault. *Tectonophysics*, 830, 229292. <https://doi.org/10.1016/j.tecto.2022.229292>
- Zohar, M., Salamon, A., & Rubin, R. (2017). Earthquake damage history in Israel and its close surrounding—Evaluation of spatial and temporal patterns. *Tectonophysics*, 696–697, 1–13. <https://doi.org/10.1016/j.tecto.2016.12.015>
- Zreda, M., & Noller, J. S. (1998). Ages of prehistoric earthquakes revealed by cosmogenic chlorine-36 in a bedrock fault scarp at Hebgen Lake. *Science*, 282(5391), 1097–1099. <https://doi.org/10.1126/science.282.5391.1097>